Electromagnetic wave absorption of coconut fiber-derived porous activated carbon

Jemilat Yetunde Yusuf[a,*], Hassan Soleimani[a,*], Noorhana Yahya[a], Yekinni Kolawole Sanusi[b], Gregory Kozlowski[c], Andreas Öchsner[d], Lawal Lanre Adebayo[a], Fatai Adisa Wahaab[a], Surajudeen Sikiru[a], Bashiru Bolaji Balogun[e]

[a] Fundamental Applied Science Department, Universiti Teknologi PETRONAS, Bandar Seri Iskandar 32610, Perak Darul Ridzuan, Malaysia
[b] Pure and Applied Physics Department, Faculty of Applied Science, Ladoke Akintola University of Technology, Ogbomosho 210214, Nigeria
[c] Physics Department, Wright State University, Dayton, OH 45435, United States
[d] Faculty of Mechanical Engineering, Esslingen University of Applied Sciences, Kanalstrasse 33, 73728 Esslingen, Germany
[e] IFIMUP and IN – Institute of Nanoscience and Nanotechnology, Department of Physics and Astronomy, University of Porto, Rua do Campo Alegre 687, 4169-007 Porto, Portugal

ARTICLE INFO

ABSTRACT

In this study, porous carbon has been prepared through potassium hydroxide (KOH) activation of coconut fiber (CF) and subsequent carbonization in the presence of an inert gas. The activated carbons (AC) were prepared via carbonization of the precursor at different temperatures. Subsequently, their electromagnetic wave absorption (EMWA) performance was investigated at X-band frequency. The phase crystallinity, porous features, and degree of graphitization of the activated carbons were studied using XRD, nitrogen adsorption/desorption isotherm, and Raman spectroscopy, respectively. Using the BET method, the activated carbon prepared at 750 °C displayed a high specific surface area of 602.9 $m^2\,g^{-1}$ and an average pore size of 6 nm, which confirms the extant of mesopores. The EMWA was studied using COMSOL Multiphysics software based on the finite element method. Results show that the activated carbon prepared at 750 °C attained an optimal reflection loss of −45.6 dB at 10.96 GHz with a corresponding effective bandwidth of 3.5 GHz at a thickness of 3.0 mm. In conclusion, this study interestingly shows that porous carbon obtained from coconut fiber has great potential for attenuating electromagnetic waves.

Absorción de ondas electromagnéticas de carbón activado poroso derivado de fibra de coco

RESUMEN

En este estudio, el carbono poroso se ha preparado mediante la activación con hidróxido de potasio (KOH) de la fibra de coco (CF) y la posterior carbonización en presencia de un gas inerte. Los carbones activados (AC) se prepararon mediante carbonización del precursor a diferentes temperaturas. Posteriormente, se investigó su rendimiento de absorción de ondas electromagnéticas (EMWA) en la frecuencia de banda X. La cristalinidad de fase, las características porosas y el grado de grafitización de los carbones activados se estudiaron utilizando XRD, isoterma de adsorción/desorción de nitrógeno y espectroscopia Raman, respectivamente. Empleando el método BET, el carbón activado preparado a 750 °C mostró una alta superficie específica de 602,9 m^2 g^{-1} y un tamaño de poro medio de 6 nm, lo que confirma la existencia de mesoporos. La EMWA se estudió utilizando el software COMSOL Multiphysics basado en el método de elementos finitos. Los resultados muestran que el carbón activado preparado a 750 °C alcanzó una pérdida de reflexión óptima de −45,6 dB a 10,96 GHz con un ancho de banda efectivo correspondiente de 3,5 GHz con un grosor de 3,0 mm. En conclusión, este estudio muestra de manera interesante que el carbono poroso obtenido de la fibra de coco tiene un gran potencial para atenuar las ondas electromagnéticas.

Introduction

Researchers have shown considerable attention toward the development of efficient microwave absorbing materials (MAMs) due to the increasing electromagnetic (EM) wave applications in electronic equipment and digital systems [1,2]. The excessive usage of electronics has made EM radiation and interference the main source of EM pollution. Therefore, a low cost and lightweight functional absorber that can successfully attenuate EM is highly required [3]. Magnetic materials and its oxides such as Co_3O_4 [4], Fe_3O_4 [5], $Ni_{0.5}Cu_{0.5}Fe_2O_4$ [6] and $Ni(OH)_2$ [7] have shown remarkable microwave absorption performance (MAP). However, certain drawbacks such as poor chemical stability and complex synthesis method limit their potential application as low-cost absorbers. Recent studies have shown that carbons obtained from agro-wastes are good candidates for microwave absorption due to their lightweight, favorable physiochemical stability, low cost, abundance, and tunable dielectric loss [8–10]. The use of carbon nanotubes (CNTs), graphene, and carbon fibers [11,12] has brought a great development to the fabrication of effective microwave absorbers due to their distinct electrical conductivity and super nanostructures [13,14]. However, the limitations of these absorbents include expensive precursors and rigorous synthesis methods that often involve the use of enormous energy and time-consuming approach [15,16]. Activated carbon (AC) from agro-waste are characterized with large surface area, good conductivity, and nano-porosity which makes them being widely used for several applications such as supercapacitors [17,18], lithium batteries [19–21], environmental protection [22,23], and EM wave absorption [24]. Thus, the use of agro-waste for the fabrication of MAMs has opened a new route toward the development of a sustainable environment and effective waste management strategy [25].

In this regard, some researchers have reported the preparation of MAMs from various agro-wastes. For instance, Wu et al. [26] successfully produced a hierarchically porous carbon (HPC) from spinach stems at different carbonization temperatures. The HPC produced at 600 °C displayed a high surface area of 345.3 m^2 g^{-1} and exhibited an optimum reflection loss (RL) of −62 dB at a thickness of 2.50 mm with corresponding effective absorption bandwidth (EAB) of 7.3 GHz. Qui et al. [27] also fabricated porous AC using walnut shells and KOH as an activating agent. The resulting porous carbon prepared at 600 °C shows a surface area of 746.2 m^2 g^{-1} and a good porous architecture compared to the non-activated carbon at 600 °C with surface area 435 m^2 g^{-1}. A minimum RL value of −42.4 dB was attained with 2.0 mm thickness sample. The favorable porosity and increased dielectric properties were reported to promote microwave absorption performance. In addition, Zhao et al. [28] prepared an AC using wheat flour as a starting material. An increase in the activation temperature greatly influences the surface area (1486.8 m^2 g^{-1}). A −51 dB minimum RL was reached at 1.8 mm with an ultralow filler content of 8% and EAB of 6 GHz. To achieve excellent MAP, the properties of carbon materials are tuned to support good impedance matching and successful attenuation of EM wave [8]. A change in the activation temperature, choice of activating agent, and impregnation ratio can regulate the dielectric properties of the AC [29]. In general, AC can be fabricated by physical or chemical activation method [30]. The former approach involves initial heating of precursors in a furnace at high temperature followed by activation of the carbonized material with steam (H_2O) or carbon dioxide (CO_2). Whereas in the latter method, the starting materials are impregnated with an activating agent (such as H_2SO_4, NaOH, $ZnCl_2$, K_2CO_3, H_3PO_4, and KOH) followed by heating at high temperature in an inert environment. Substantially, studies have shown that AC produced via chemical activation often possess a relatively

higher specific surface area and more micro-scale pores than those produced by physical activation [31–35]. KOH has been widely used in the preparation of AC due to the well-developed pores and large surface area of obtained samples [31,34,35]. An increase in carbonization temperature often results in increased carbon content, surface area, pore volume, and pore sizes of the ACs [36]. The carbonization temperature during the preparation of the chemically AC plays a significant role in its EM wave absorption performances. The pores (microscale) enhances multi-reflection and scattering of the EM waves, reduces bulk density, and improves impedance matching [37]. The large specific surface area is also beneficial for the successful attenuation of EM wave thereby enhancing microwave absorption performance [38].

In this work, porous carbon has been prepared using coconut fiber as an agro-waste precursor. The coconut fiber was impregnated by KOH as an activating agent and the slurry was carbonized at different temperatures in an inert atmosphere. COMSOL Multiphysics was employed to study the EM wave absorption of coconut fiber-derived porous activated carbon (CFAC). Results show that the CFAC prepared at 750 °C achieved minimum RL peak value of □45.6 dB at 10.96 GHz frequency with a corresponding sample thickness of 3.0 mm and EAB of 3.5 GHz. The findings adequately affirm porous carbon from agro-waste as potential MAMs at X-band frequency.

Experimental

Preparation of activated carbon

Coconut husks were collected from local markets and the coconut fibers (CF) were extracted from the husk. The CFs were rinsed using deionized (DI) water, sun-dried for 8 h, and subsequently dried overnight at 75 °C. The sun-dried sample was grounded into powder using a mechanical grinding process. To prepare KOH solution, 20 g of KOH pellet were dissolved in 50 mL DI water. The ground CF was then impregnated in the KOH solution by adding 20 g of CF powder in 50 mL KOH solution and continuously stirred for 6 h at a temperature of 65 °C. The slurry was allowed to age for 6 h and dried overnight in an oven at a temperature of 80 °C. 20 g of pretreated CF samples were then carbonized in a tube furnace at 550 °C, 650 °C, and 750 °C for 2 h at 5 °C min^{-1} under N$_2$ atmosphere. The samples were labeled CFAC@550, CFAC@650, and CFAC@750, respectively. The resulting samples were purified several times with 0.1 M HCl and deionized water until a pH of 7 is attained. The washed AC samples were subsequently oven dried for 8 h at 100 °C, left to cool to room temperature, and finally transferred into a closed sample holder to prevent pore blockage that could arise from atmospheric gasses adsorption.

Characterization

The phase crystallinities were characterized using an X-ray diffraction spectrometer (Cu Kα radiation source, 40.0 mA, λ = 0.15406 nm, 45 kV). To study the kind of carbon in the samples, Raman spectra were also studied using the Renishaw Invia Raman spectrometer (λ = 514 nm). Carbon, Hydrogen, Nitrogen, Sulphur, and Oxygen (CHNSO) Elemental Analyzer

was used to study the Elemental composition. Micrometrics ASAP 2020 was used to study the Brunauer Emmett and Teller (BET) surface and pore analysis. The BET technique uses the adsorption/desorption of N$_2$ gas on the surface of the samples to determine their surface area and pore characteristics. Mercury porosimetry was further used to analyze the pore size and the pore volume of the samples. A four-point-probe technique was used to determine the electrical conductivity of the CFAC Samples. 50 wt% of the CFAC samples were homogenously mixed in paraffin wax solution for EM measurement. The EM properties were measured at X-band frequency with Keysight (E5071C) vector network analyzer using the rectangular waveguide method. The measured properties were used in COMSOL Multiphysics for study of the microwave absorption properties at X-band frequency.

Finite element method (FEM)

The scattering parameters of the CFAC samples filled in rectangular waveguide were simulated with COMSOL Multiphysics software based on FEM. The WR 90 rectangular waveguide was modeled in three-dimension geometry with schematic illustrated in Fig. 1.

In geometry modeling, the waveguide was partitioned into three domains. The first and third domains were air-filled. The second region was filled with measured material properties. The rectangular waveguide boundaries were treated as perfect electric conductor (PEC), aside two boundaries of wave excitation denoted as port 1 and port 2. Then, a mesh consisting of triangles is created with the number of triangles increasing with the density of the material properties as can be seen in Fig. 1. Next, port boundary of the RF module was employed for wave excitation and the transverse electric TE$_{10}$ mode was made to propagate through the WR 90 waveguide.

Based on Maxwell's equation, the wave equation for electric field "E" propagating through the waveguide is as given in Eq. (1):

$$\nabla \times \mu_r^{-1}(\nabla \times E) - k_o{}^2 \left(\varepsilon_r - \frac{j\sigma}{\omega\varepsilon_o} \right) = 0 \qquad (1)$$

where ε_r is the relative complex permittivity, σ is the conductivity, ω is the angular velocity; $2\pi f$ (f = frequency), μ_r is the relative complex permeability, ε_o is free space permittivity and k is the wave vector. Following FEM modulation, the electric field in the simulated waveguide is discretized via tetrahedron meshes [16,17]. Thus, the EM field within individual elements is interpolated from each node value with the first-order polynomial given below in Eq. (2):

$$\rho^e(x, y, z) = a^e + b^e{}_X + c^e{}_y + d^e{}_Z \qquad (2)$$

The equation for the electric field (E^e) in the rectangular waveguide based on FEM is given in Eq. (3) as follows:

$$E^e = \sum_{i=1}^{6} N_i^e E_i^e(x.y.z) \qquad (3)$$

where $N_i^e = 1, 2, 3 \cdots 6$ are the complex parameters of the electric field E-Field which correlates with the elements six edges.
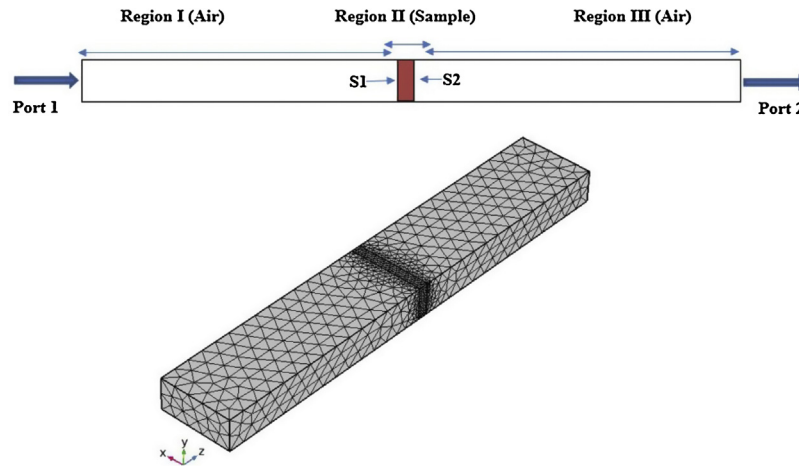
Fig. 1 – Schematic of rectangular waveguide loaded with CFAC sample and mesh of a rectangular waveguide loaded with CFAC sample.

The $E_i^e(x, y, z)$ is a vector function that relates to the ith point of an element. The integral over one element volume by applying boundary conditions is given in (4):

$$\frac{1}{\mu_r} \cdot \sum_{i=1}^{6} N_i^e \iiint (\nabla \times W_j . \nabla \times W_i - K_0^2 \varepsilon_r W_i . W_j) dv 2 \left(\frac{jw\mu}{\mu_r} \right).$$

$$Y_0^I . \iint W_j . e_o(x, y) ds - \left(\frac{jw\mu}{\mu_r} \right) \sum_{i=1}^{6} N_i^e \sum_{p=0}^{\infty} Y_p^I$$

$$\left(\iint W_j e_p(x, y) ds . \iint W_i . e_p(x, y) ds \right) \quad (4)$$

Simplification of Eq. (4) gives the matrix equation as written below in Eq. (5):

$$\begin{pmatrix} S_{11}^e & \cdots & S_{16}^e \\ \vdots & \ddots & \vdots \\ S_{61}^e & \cdots & S_{66}^e \end{pmatrix} \begin{bmatrix} N_1^e \\ \vdots \\ N_6^e \end{bmatrix} = \begin{bmatrix} V_1^e \\ \vdots \\ V_6^e \end{bmatrix} \quad (5)$$

The elements of the above matrices are expressed below in Eqs. (6) and (7).

$$S_{e1}(j, i) = \frac{1}{\mu_r} \iiint (\nabla \times W_j \times \nabla \times W_i - K_0^2 \varepsilon_r W_i \times W_j) dv$$

$$+ \left(\frac{jw\mu}{\mu_r} \right) \sum_{p=0}^{\infty} Y_0^I \left(\iint W_j \times e_p(x, y) ds . \iint W_i \times e_p(x, y) ds \right) \quad (6)$$

$$V(j) = 2 \left(\frac{jw\mu}{\mu_r} \right) \times Y_0^I \iint W_i \times e_0(x, y) ds \quad (7)$$

where V is derived via boundary conditions. The element matrices are amassed over all tetrahedron elements of the
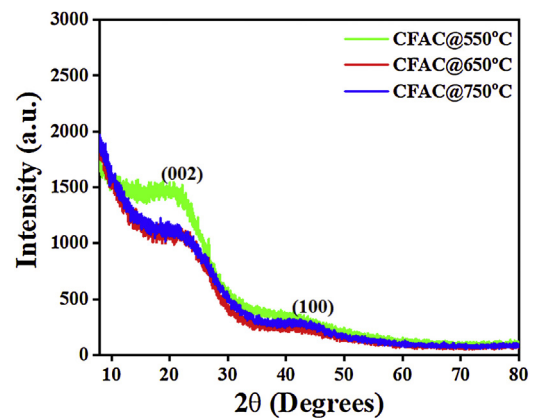

Fig. 2 – XRD patterns of CFAC samples.

segment filled with CFAC sample to obtain the final matrix equation as shown in Eq. (8):

$$[S] \times \{N_I\} = \{V\} \quad (8)$$

At this point, the software uses the solution obtained from Eq. (8) to evaluate the reflection and transmission coefficient of the CFAC samples.

Results and discussion

Phase crystallinity

The XRD patterns of all the CFAC samples is as presented in Fig. 2. All samples display two peaks centered at 24.5° and 44.1° and these peaks correspond to the (0 0 2) and (1 0 0) crystal planes of graphite [9]. This affirms the formation of graphite like structure of amorphous carbon in the CFAC samples.
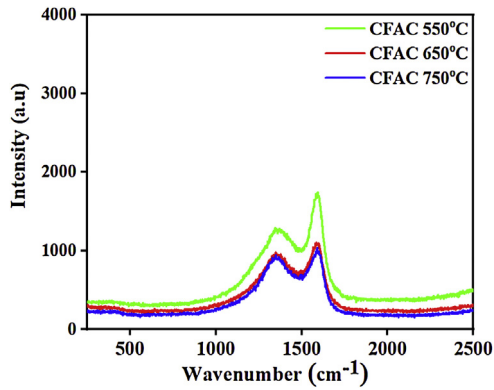
Fig. 3 – Raman spectra of CFAC samples.

Raman spectra

To further investigate the type of carbon present in the samples. Fig. 3 shows the Raman spectra obtained for CFAC samples at different temperatures. All samples exhibit two conspicuous peaks located at 1349 cm^{-1} and 1594 cm^{-1} which corresponds to the disordered carbon (D-band) and in plane of sp^2 hybridized carbon atom (G-band) band, respectively. The D-bands represent the out of plane sp^3 hybridized vibration of carbon atom, whereas the G-band indicates the characteristic in-plane vibration of sp^2 hybridized carbon atom [39]. The degree of graphitization (I_D/I_G) is studied to evaluate the defect ratio and extent of graphitization of the carbonaceous materials [40]. It was observed that the I_D/I_G increases with increasing temperature. This is due to the improved crystallinity as the temperature increases. The I_D/I_G ratio of CFAC@550, CFAC@650, and CFAC@750 are evaluated as 0.84, 0.86 and 0.87, respectively. CFAC@750 has higher graphitization degree that indicates that the sample contains more defects which is beneficial for a rapid attenuation of EMW.

Pore size distribution

The porous nature and pore size distribution of the CFAC absorbers are analyzed by measuring the N$_2$ adsorption/desorption isotherm. Fig. 4a–c displays open-ended type II with hysteresis curve within 0.5–1.0 relative pressure range and Fig. 4d displays the plots of mercury porosimetry of the CFAC samples. The low-adsorption at lower relative pressure in all the samples and openings in Fig. 4a and b have been reported to arise from incomplete combustion in the carbonization process resulting in pore reduction [41]. This shows that micropores are predominant within the samples [42]. The adsorption shows that a strong interaction exists between the sample surface and adsorbate. The rapid rise in nitrogen uptake at a low relative pressure (0.0–0.9) indicates micropore adsorption [27]. KOH activation has been known to produce abundant pore networks in CFAC samples. Etching of carbon precursor with KOH through redox reaction leads to formation of copious micro/mesopores based on the following reactions between 400 °C and 500 °C. The KOH reacts with the carbon
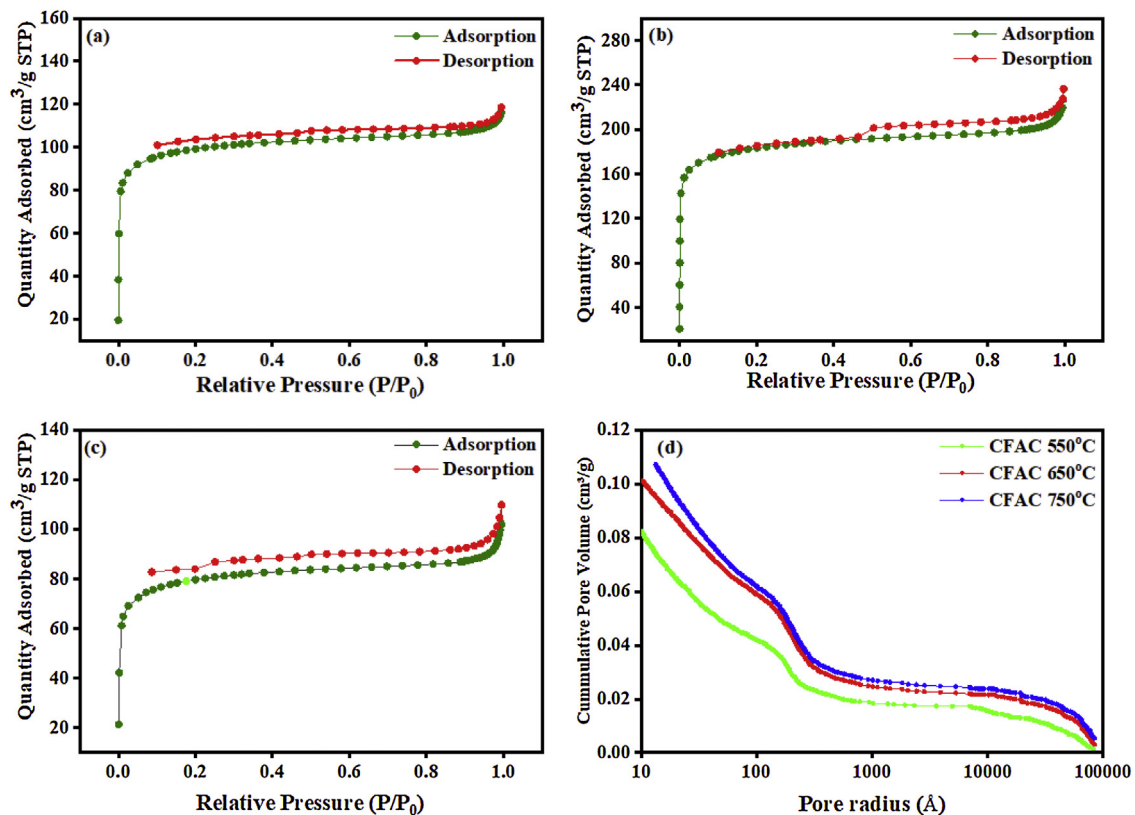
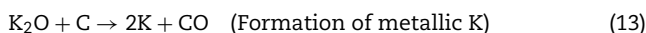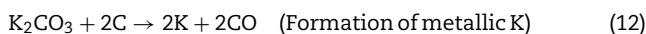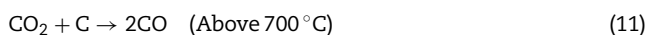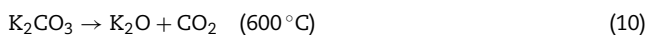**Fig. 4 – (a–c) N$_2$ adsorption–desorption isotherm curves of CFAC samples and (d) plot of mercury porosimetry of the CFAC samples.**

Table 1 – Surface BET, pore volume and pore size of CFAC samples at different temperature.

| Samples	N$_2$ adsorption			Mercury porosimetry		
	S$_{BET}$ (m^2 g^{-1})	TPV$_{N2}$ (cm^3 g^{-1})	Pore size (nm)	TPV$_{Me}$ (mm^3 g^{-1})	TPV$_{Me}$ (cm^3 g^{-1})	Pore size (nm)
CFAC@550	260.25	0.056	5.3	52.98	0.053	7.27
CFAC@650	323.78	0.041	5.5	68.63	0.069	9.03
CFAC@750	602.87	0.104	6.6	84.27	0.084	12.39

TPV: total pore volume; N$_2$: nitrogen; Me: mercury; nm: nanometer; S$_{BET}$: surface Braunauer Emmert Teller.

precursors to produce H$_2$ and K$_2$CO$_3$ as the product of the reaction as given in Eq. (9):

$$6KOH + 2C \rightarrow 2K + 3H_2 + 2K_2CO_3 \quad (400–500\,°C) \qquad (9)$$

$$K_2CO_3 \rightarrow K_2O + CO_2 \quad (600\,°C) \qquad (10)$$

$$CO_2 + C \rightarrow 2CO \quad (Above\ 700\,°C) \qquad (11)$$

$$K_2CO_3 + 2C \rightarrow 2K + 2CO \quad (Formation\ of\ metallic\ K) \qquad (12)$$

$$K_2O + C \rightarrow 2K + CO \quad (Formation\ of\ metallic\ K) \qquad (13)$$

KOH is completely consumed when the temperature is increased close to 600 °C. The K$_2$CO$_3$ produced from Eq. (9), then decompose at temperatures higher than 600 °C to produce CO$_2$ and K$_2$O as shown in Eq. (10). The formation of CO$_2$ and H$_2$ through the activation activity also promotes the development and distribution of pores because of the carbon (C) gasification. At a temperature above 700 °C, the resulting CO$_2$ is reduced by C to form CO as depicted in Eq. (11). Subsequently, K$_2$CO$_3$ and K$_2$O also reduce by C to produce metallic K as shown in Eqs. (12) and (13). The metallic K forms effective intercalation into the carbon lattice creating an expansion in the carbon lattice [43]. During neutralization, the metallic K is washed away, and then the carbon surface and interior cavity get eroded. This induces an irreversible expansion to the lattice of the AC produced, thereby generating highly developed pores and large surface area [43]. The pores can effectively trap EM waves, resulting in accumulation of charges at the interface causing interfacial polarization which will enhance EM absorption.

Table 1 reveals pore size distribution of the CFAC for nitrogen adsorption and mercury porosimetry analyses. The BET surface area, total pore volume and pore size of the samples shows that the carbonization temperature has an impact on the porous network and surface area of the CFAC samples. The S$_{BET}$ increases with an increase in temperature likewise the pore sizes also increase. Liu et al. [44] reported that the surface area and pore size can influence the scattering parameter in EM absorption. The large surface area of CFAC@750 is expected to have abundant charges which would favor the rapid attenuation of EM wave more than the CFAC@650 and CFAC@550. The high pore size and pore volume in CFAC@750 would also enhances multireflection and scattering of the EM waves which will enhance microwave absorption performance [44–46]. Mercury porosimetry uses air as the wetting fluid and mercury as the nonwetting fluid. Mercury is forced into the pores of the CFAC samples incrementally. The variation
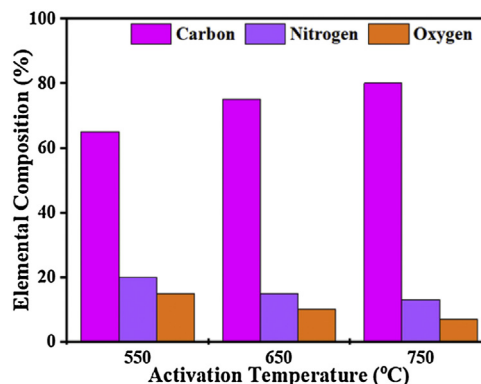
Fig. 5 – Elemental compositions (carbon, nitrogen, and oxygen) percentage of CFAC.

between the pore radius of the samples and the cumulative pore volume (mercury porosimetry) is as displayed in Fig. 4d. The relatively high total pore volume (TPV$_{Me}$) of CFAC@750 indicates the presence of mesopores during heat treatment of the chemically activated samples. The mercury density decreases with increasing temperature, which is consistent with an increase in the development of porosity in the carbons [47]. Like the observation from Nitrogen adsorption analysis, the mercury porosimetry also showed increased pore size with increase in carbonatization temperature for the CFAC samples.

The elemental composition of CFAC samples was affected by the carbonization temperature as displayed in Fig. 5. Carbon yield (%) increases with an increase in the pyrolysis temperature whereas, the low nitrogen content and oxygen are due to a decrease in defects [48]. Therefore, at high temperatures, a large number of free conduction electrons are present which in turn drives out heteroatoms from the carbon atoms [49]. The resulting C–C interacts, thereby resulting in improved conductivity which favors the absorption of EM wave [50].

Surface morphology

The FESEM images presented in Fig. 6 show the surface morphology of the CFAC samples. The surface morphology of CFAC@550 in Fig. 6a–c reveals the presence of poorly developed and sparsely distributed pores with deformed surface and cracked wall. Fig. 6d reveals the estimated pore size and surface area of CFAC@550 measured with FESEM. The poor porosity of CFAC@550 can be ascribed to relatively low activation temperature and pore blockage from impurities [51]. Whereas CFAC@650 reveals the presence numerous
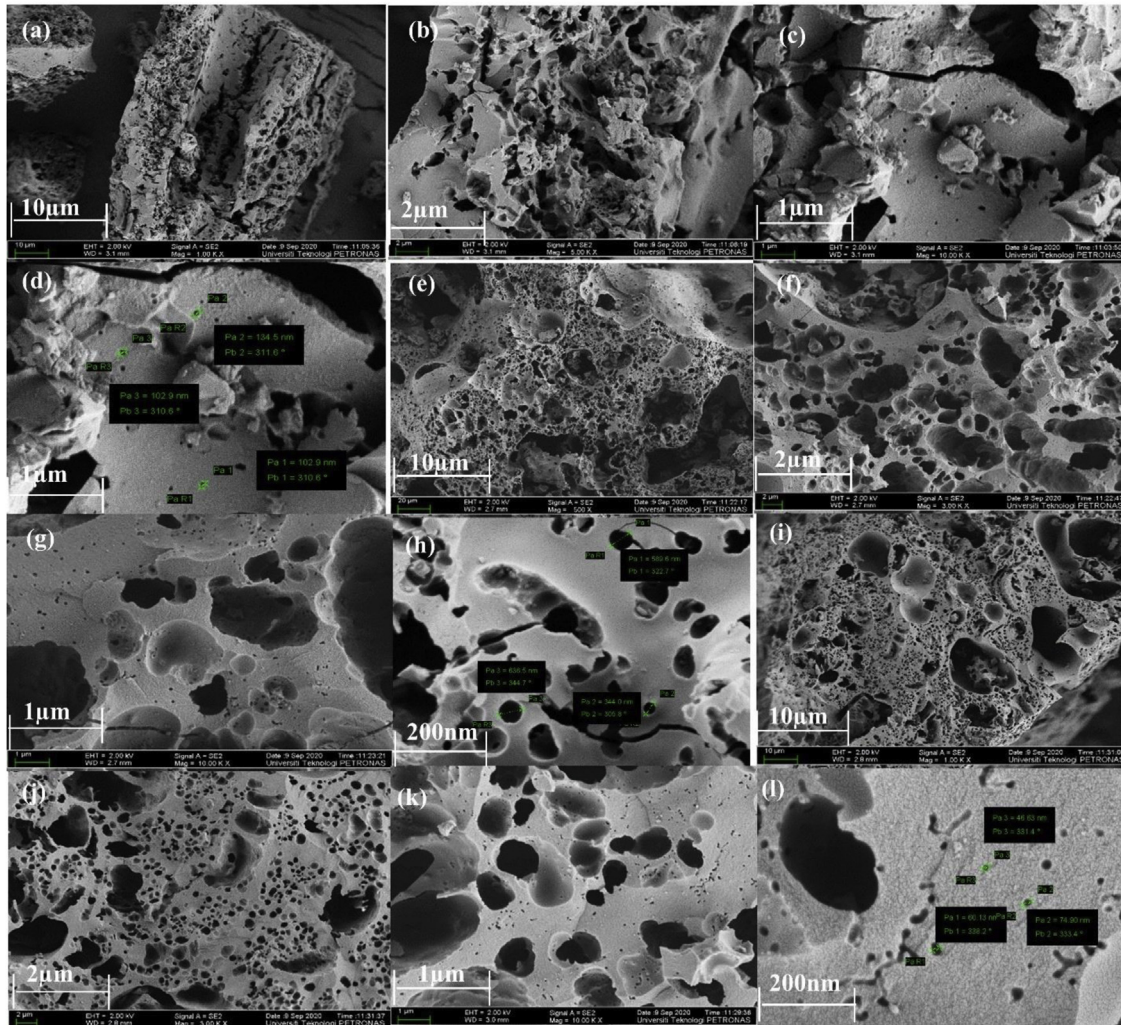
Fig. 6 – FESEM characterization of (a–d) CFAC@550, (e–h) CFAC@650 and (i–l) CFAC@750.

well-developed pores as observed in Fig. 6e–h. CFAC@750 shows a well-developed pore size as observed in Fig. 6i–l. The well-developed pores in both CFAC@650 and CFAC@750 can be ascribed to etching of the CFAC samples with KOH and carbonization at relatively high temperature compared to CFAC@550. This indicates that at higher temperature, the porosity of the sample increased. CFAC@650 shows irregular pores randomly distributed on the surface of the sample. Also, the presence of cracks in the carbon matrix of CFAC@650 can be ascribed to thermal stress [52]. Likewise, CFAC@750 also contains small irregular pores randomly distributed on the surface of the sample. The presence of numerous pores in CFAC@650 and CFAC@750 samples will allow multi-reflection and scattering of EM waves within the samples thereby promoting enhanced EM wave absorption.

Electrical conductivity

The intrinsic electrical conductivity (σ) is an essential parameter that can influence the EMWA ability of MAMs. In carbon materials, the nature of electron transport is proportional to the degree of crystallinity [53]. As shown in Fig. 7, the values of
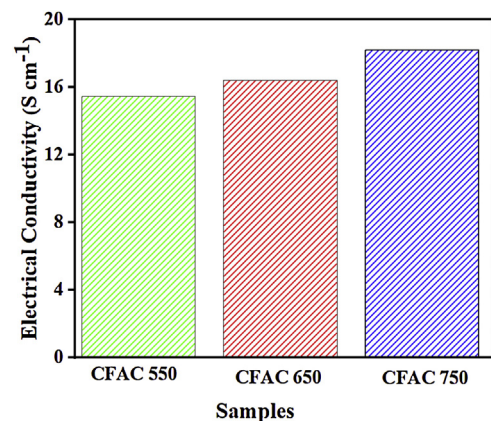

Fig. 7 – Electrical conductivity of CFAC samples.

electrical conductivity exhibit certain regularity with respect to the carbonization temperature of the CFAC samples. The σ value increases stepwise as the carbonization temperature increases. This indirectly verifies that the crystalline volume fraction has been enlarged through chemical activation of the
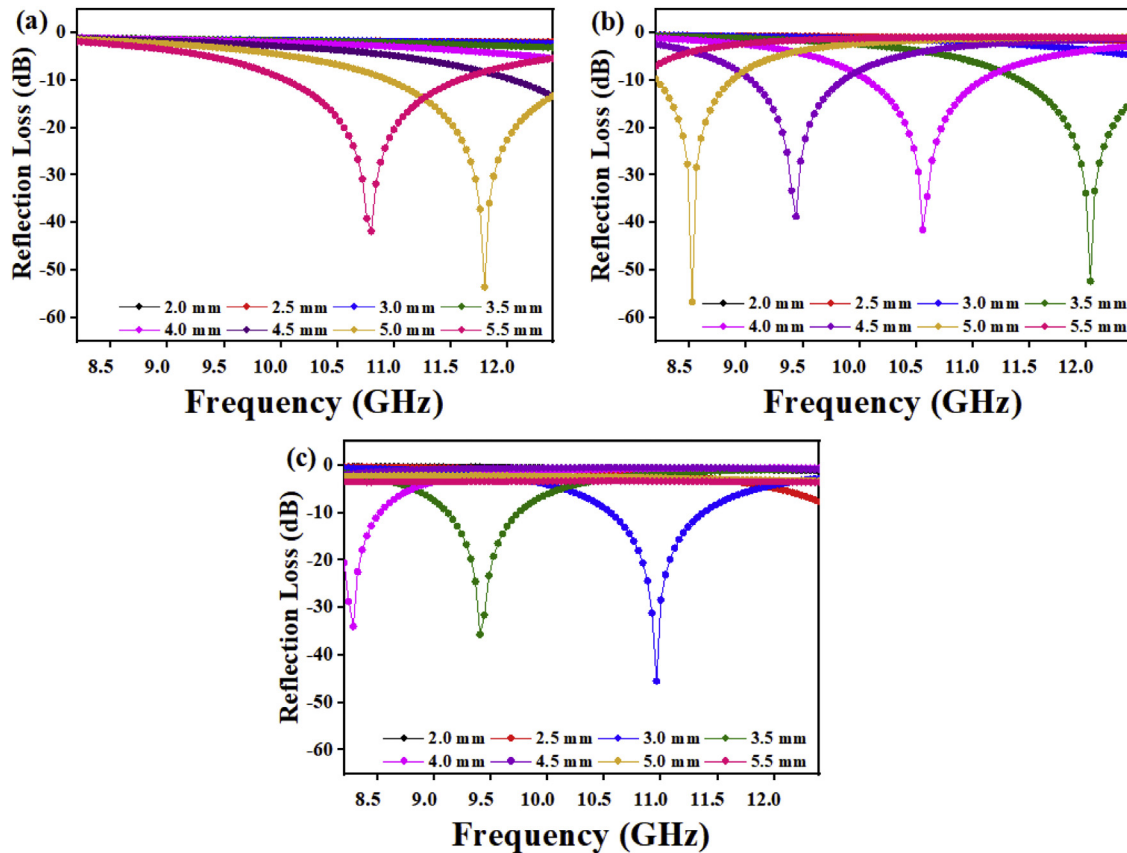
Fig. 8 – Reflection loss graph of (a) CFAC@550, (b) CFAC@650, and (c) CFAC@750.

CFAC before carbonization [54]. For CFAC@750, the σ was measured as $18.23\,S\,cm^{-1}$, which was superior to the CFAC@650 and CFAC@550. Therefore, the σ values indicates that CFAC samples have good electrical conductivity thereby creating an efficient electrical relaxation route for the incoming EM waves which results in deterioration of the EM waves [55] within the CFAC samples.

Electromagnetic wave absorption properties

Using the simulated reflection coefficients and according to the transmission line theory [56], absorption coefficients generally regarded as RL of the samples were evaluated from Eqs. (14)–(16):

$$Z_{in} = Z_o \sqrt{\frac{\varepsilon_r}{\mu_r}} \tan h \left(j \frac{2\pi f d}{c} \sqrt{\varepsilon_r \mu_r} \right) \qquad (14)$$

$$RL(dB) = 20 \log_{10}[] \qquad (15)$$

$$= \frac{Z_{in} - Z_O}{Z_{in} + Z_0} \qquad (16)$$

where Z_o is the free space impedance, f represents the microwave frequency, ε_r denotes the relative permittivity, μ_r is the complex permeability, d symbolizes the absorber thickness, c represents the velocity of EM wave propagation in vacuum, Z_{in} indicates absorbers impedance, and Γ represents the reflection coefficient. The absorption curves of CFAC samples at absorber thicknesses ranging from 2.0 to 5.5 mm at X-band frequency is as shown in Fig. 8. The microwave absorption properties of the samples were enhanced with the increase in carbonization temperature. Fig. 8a (CFAC@550) displayed a minimum RL peak value of −41.8 dB at 10.8 GHz with a matching thickness of 5.5 mm and EAB of 2.5 GHz. At 5.0 mm matching thickness, the sample achieved an optimal RL value of −53.55 dB with a narrow bandwidth of 0.8 GHz, which does not meet the requirement of an ideal absorber. CFAC@650 achieved a minimum RL value of −41.6 dB at 10.56 GHz with a matching thickness of 4.0 mm and relatively broad EAB of 4.0 GHz (Fig. 8b). For CFAC@750 presented in Fig. 8c, a minimum RL peak value of −45.6 dB was obtained at 10.96 GHz at a reduced thickness of 3.0 mm with EAB of 3.5 GHz.

Table 2 presents the MAP of porous carbon absorber derived from agro-waste reported in the literature. It was observed that the porous carbon reported in this study exhibit good microwave absorbing properties as compared with the literature. The improved absorption of CFAC@650 and CFAC@750 could be ascribed to the increased number of pores and surface areas which improve multiple reflection and attenuation of EMW.

Table 2 – Microwave absorption properties of some porous carbon absorbers derived from biomass in recent years.						
Absorbers	Loading (%)	Frequency(GHz)	Minimum RL (dB)	EAB(GHz)	Thickness(mm)	Ref.
Walnut shell NPC	30%	8.2	−36.9	6.3	3.5	[27]
Walnut shell NPC	30%	8.8	−42.4	1.7	2.0	[9]
WPC 600	50%	7.4	−33.6	1.7	NA	[57]
Wheat flour AC	8%	15.8	−43.0	4.8	2.7	[28]
Spinach stem HPC 600 °C	30%	7.3	−62.2	7.3	2.7	[26]
Spinach leaf HPC 700 °C	50%	7.3	−22.6	7.8	2.5	[26]
Cabbage stem	50%	NA	−52.8	5.1	2.4	
Cabbage leaf	30%	NA	−41.4	5.1	2.5	[26]
Coconut fiber	50%	10.96	−45.6	3.59	3.0	This study

NA: not available; EAB: effective absorption bandwidth; RL: reflection loss; WPC: walnut porous carbon; NPC: nano porous carbon; AC: activated carbon; HPC: hierarchically porous carbons.

Conclusion

The microwave absorption of the CFAC samples were studied. The precursor was prepared via chemical activation with KOH and carbonized at 550 °C, 650 °C, and 750 °C. The resulting AC showed distinct porosity and large surface area with CFAC@750 having the highest pore size and largest surface area. The MAP was studied with COMSOL Multiphysics based on FEM. The variation in the carbonization temperature was found to regulate the MAP of CFAC absorbers. CFAC carbonized at 750 °C showed excellent microwave absorption performance with a minimum RL peak value of −45.6 dB at 10.96 GHz with a 3.0 mm thickness. The good absorption performance of CFAC at elevated temperature can be attributed to good conduction loss and interfacial polarization. The numerous numbers of pores also induce multiple reflections of microwave through high conductivity. Therefore, it is reasonable to conclude that CFAC sample can be a good candidate for effective absorption of EM wave at X band frequency.

Competing interest

The authors declare that they have no known competing financial interests or personal relationships that could have appeared to influence the work reported in this paper.

Acknowledgements

REFERENCES

[1] R. Panwar, S. Puthucheri, D. Singh, et al., Microwave absorption properties of FSS-impacted composites as a broadband microwave absorber, Adv. Compos. Mater. 26 (2) (2016) 99–113, http://dx.doi.org/10.1080/09243046.2016.1232009.

[2] F. Qin, C. Brosseau, A review and analysis of microwave absorption in polymer composites filled with carbonaceous particles, J. Appl. Phys. 111 (6) (2012), http://dx.doi.org/10.1063/1.3688435.

[3] L.L. Adebayo, H. Soleimani, N. Yahya, et al., Recent advances in the development of Fe_3O_4-based microwave absorbing materials, Ceram. Int. 46 (2) (2019) 1249–1268, http://dx.doi.org/10.1016/j.ceramint.2019.09.209.

[4] I. Abdalla, J. Shen, J. Yu, et al., Co_3O_4/carbon composite nanofibrous membrane enabled high-efficiency electromagnetic wave absorption, Sci. Rep. 8 (1) (2018) 12402, http://dx.doi.org/10.1038/s41598-018-30871-2.

[5] L.L. Adebayo, H. Soleimani, N. Yahya, et al., Investigation of the broadband microwave absorption of citric acid coated Fe_3O_4/PVDF composite using finite element method, Appl. Sci. 9 (18) (2019), http://dx.doi.org/10.3390/app9183877.

[6] F.A. Wahaab, L.L. Adebayo, A.A. Adekoya, et al., Physiochemical properties and electromagnetic wave absorption performance of $Ni_{0.5}Cu_{0.5}Fe_2O_4$ nanoparticles at X-band frequency, J. Alloys Compd. 836 (2020) 155272, http://dx.doi.org/10.1016/j.jallcom.2020.155272.

[7] J. Liu, M.S. Cao, Q. Luo, et al., Electromagnetic property and tunable microwave absorption of 3D nets from nickel chains at elevated temperature, ACS Appl. Mater. Interfaces 8 (34) (2016) 22615–22622, http://dx.doi.org/10.1021/acsami.6b05480.

[8] H. Zhao, Y. Cheng, W. Liu, et al., Biomass-derived porous carbon-based nanostructures for microwave absorption, Nano-Micro Lett. 11 (24) (2019), http://dx.doi.org/10.1007/s40820-019-0255-3.

[9] P. Zhou, X. Wang, L. Wang, et al., Walnut shell-derived nanoporous carbon@Fe3O4 composites for outstanding microwave absorption performance, J. Alloys Compd. 805 (2019) 1071–1080, http://dx.doi.org/10.1016/j.jallcom.2019.07.177.

[10] H. Xu, X. Yin, M. Zhu, et al., Carbon hollow microspheres with a designable mesoporous shell for high-performance electromagnetic wave absorption, ACS Appl. Mater. Interfaces 9 (7) (2017) 6332–6341, http://dx.doi.org/10.1021/acsami.6b15826.

[11] W. Li, H. Qi, F. Guo, et al., Co nanoparticles supported on cotton-based carbon fibers: a novel broadband microwave absorbent, J. Alloys Compd. 772 (2019) 760–769, http://dx.doi.org/10.1016/j.jallcom.2018.09.075.

[12] H. Liu, Y. Li, M. Yuan, et al., In situ preparation of cobalt nanoparticles decorated in N-doped carbon nanofibers as excellent electromagnetic wave absorbers, ACS Appl. Mater. Interfaces 10 (26) (2018) 22591–22601, http://dx.doi.org/10.1021/acsami.8b05211.

[13] Y. Ding, Z. Zhang, B. Luo, et al., Investigation on the broadband electromagnetic wave absorption properties and mechanism of Co_3O_4-nanosheets/reduced-graphene-oxide composite, Nano Res. 10 (3) (2017) 980–990, http://dx.doi.org/10.1007/s12274-016-1357-6.

[14] M. Cao, C. Han, X. Wang, et al., Graphene nanohybrids: excellent electromagnetic properties for the absorbing and shielding of electromagnetic waves, J. Mater. Chem. C 6 (17) (2018) 4586–4602, http://dx.doi.org/10.1039/C7TC05869A.

[15] A. Nazir, H. Yu, L. Wang, et al., Recent progress in the modification of carbon materials and their application in composites for electromagnetic interference shielding, J. Mater. Sci. 53 (12) (2018) 8699–8719, http://dx.doi.org/10.1007/s10853-018-2122-x.

[16] C. Luo, Y. Tang, T. Jiao, et al., High-temperature stable and metal-free electromagnetic wave absorbing SiBCN ceramics derived from carbon-rich hyperbranched polyborosilazanes, ACS Appl. Mater. Interfaces 10 (1) (2018) 28051–32806, http://dx.doi.org/10.1021/acsami.8b07879.

[17] H. Wei, H. Wang, A. Li, et al., Advanced porous hierarchical activated carbon derived from agricultural wastes toward high performance supercapacitors, J. Alloys Compd. 820 (2020) 153111, http://dx.doi.org/10.1016/j.jallcom.2019.153111.

[18] F. Cheng, X. Yang, S. Zhang, et al., Boosting the supercapacitor performances of activated carbon with carbon nanomaterials, J. Power Sources 450 (2020) 227678, http://dx.doi.org/10.1016/j.jpowsour.2019.227678.

[19] F. Markoulidis, J. Bates, C. Lekakou, et al., Supercapacitors with lithium-ion electrolyte: an experimental study and design of the activated carbon electrodes via modelling and simulations, Carbon 164 (2020) 422–434, http://dx.doi.org/10.1016/j.carbon.2020.04.017.

[20] K. Yu, J. Wang, X. Wang, et al., Sustainable application of biomass by-products: corn straw-derived porous carbon nanospheres using as anode materials for lithium ion batteries, Mater. Chem. Phys. 243 (2020) 122644, http://dx.doi.org/10.1016/j.matchemphys.2020.122644.

[21] M. Zhang, J. Cheng, L. Zhang, et al., Activated carbon by one-step calcination of deoxygenated agar for high voltage lithium ion supercapacitor, ACS Sust. Chem. Eng. 8 (9) (2020) 3637–3643, http://dx.doi.org/10.1021/acssuschemeng.9b06347.

[22] A. Sanyal, J. Behari, Electromagnetic pollution – the causes and concerns, in: Proceedings of INCEMIC, 2001–2002, pp. 316–320, http://dx.doi.org/10.1109/ICEMIC.2002.1006546.

[23] Z. Cai, X. Deng, Q. Wang, et al., Core–shell granular activated carbon and its adsorption of trypan blue, J. Clean. Prod. 242 (2020) 118496, http://dx.doi.org/10.1016/j.jclepro.2019.118496.

[24] J. Deng, M. Li, Y. Wang, Biomass-derived carbon: synthesis and applications in energy storage and conversion, Green Chem. 18 (2016) 4824–4854, http://dx.doi.org/10.1039/c6gc01172a.

[25] G. Xu, J. Han, B. Ding, et al., Biomass-derived porous carbon materials with sulfur and nitrogen dual-doping for energy storage, Green Chem. 17 (3) (2015) 1668–1674, http://dx.doi.org/10.1039/c4gc02185a.

[26] Z. Wu, K. Tian, T. Huang, et al., Hierarchically porous carbons derived from biomasses with excellent microwave absorption performance, ACS Appl. Mater. Interfaces 10 (13) (2018) 11108–11115, http://dx.doi.org/10.1021/acsami.7b17264.

[27] X. Qiu, L. Wang, H. Zhu, et al., Lightweight and efficient microwave absorbing materials based on walnut shell-derived nano-porous carbon, Nanoscale 9 (22) (2017) 7408–7418, http://dx.doi.org/10.1039/C7NR02628E.

[28] H. Zhao, Y. Cheng, B.Z.H. Lv, et al., Achieving sustainable ultralight electromagnetic absorber from flour by turning surface morphology of nanoporous carbon, ACS Sustain. Chem. Eng. 6 (11) (2018) 15850–15857, http://dx.doi.org/10.1021/acssuschemeng.8b04461.

[29] C. Li, Y. Ge, X. Jiang, et al., Porous Fe_3O_4/C microspheres for efficient broadband electromagnetic wave absorption,

[30] H. Zhang, Y. Yan, L. Yang, Preparation of activated carbons from sawdust by chemical activation, Adsorp. Sci. Technol. 26 (7) (2008) 533–543, http://dx.doi.org/10.1260/0263-6174.26.7.533.

[31] H. Zhao, Y. Cheng, W. Liu, et al., Biomass-derived porous carbon-based nanostructures for microwave absorption, Nano-Micro Lett. 11 (1) (2019), http://dx.doi.org/10.1007/s40820-019-0255-3.

[32] J. Deng, M. Li, Y. Wang, Biomass-derived carbon: synthesis and applications in energy storage and conversion, Green Chem. 18 (18) (2016) 4824–4854, http://dx.doi.org/10.1039/C6GC01172A.

[33] P.T. Williams, A.R. Reed, Development of activated carbon pore structure via physical and chemical activation of biomass fibre waste, Biomass Bioenergy 30 (2) (2006) 144–152, http://dx.doi.org/10.1016/j.biombioe.2005.11.006.

[34] I.I.G. Inal, S.M. Holmes, A. Banford, et al., The performance of supercapacitor electrodes developed from chemically activated carbon produced from waste tea, Appl. Surf. Sci. 357 (2015) 696–703, http://dx.doi.org/10.1016/j.apsusc.2015.09.067.

[35] El-Hendawy, A. Abdel-Nasser, An insight into the KOH activation mechanism through the production of microporous activated carbon for the removal of Pb^{2+} cations, Appl. Surf. Sci. 255 (6) (2009) 3723–3730, http://dx.doi.org/10.1016/j.apsusc.2008.10.034.

[36] O.F. Olorundare, T.A.M. Msagati, R.W.M. Krause, et al., Activated carbon from lignocellulosic waste residues: effect of activating agent on porosity characteristics and use as adsorbents for organic species, Water Air Soil Pollut. 225 (1876) (2014) 1–14, http://dx.doi.org/10.1007/s11270-014-1876-2.

[37] H. Lv, X. Liang, et al., Porous three-dimensional flower-like Co/CoO and its excellent electromagnetic absorption properties, ACS Appl. Mater. Interfaces 7 (18) (2015) 9776–9783, http://dx.doi.org/10.1021/acsami.5b01654.

[38] J. Fang, T. Liu, Z. Chen, et al., A wormhole-like porous carbon/magnetic particles composite as an efficient broadband electromagnetic wave absorber, Nanoscale 8 (16) (2016) 8899–8909, http://dx.doi.org/10.1039/C6NR01863G.

[39] T. Yang, T. Qian, M. Wang, et al., A sustainable route from biomass byproduct okara to high content nitrogen-doped carbon sheets for efficient sodium ion batteries, Adv. Mater. 28 (3) (2016) 539–545, http://dx.doi.org/10.1002/adma.201503221.

[40] R.J. Nemanich, S.A. Solin, First- and second-order Raman scattering from finite-size crystals of graphite, Phys. Rev. B: Condens. Matter Mater. Phys. 20 (1979) 392–401.

[41] A. Allwar, Preparation and characteristics of highly microporous activated carbon derived from empty fruit bunch of palm oil using KOH activation, Rasāyan J. Chem. 11 (1) (2018) 280–286, http://dx.doi.org/10.7324/RJC. 2018.1112000.

[42] G. Li, Y. Li, J. Chen, et al., Synthesis and research of egg shell-yolk NiO/C porous composites as lithium-ion battery anode material, Electrochim. Acta 245 (2017) 941–948, http://dx.doi.org/10.1016/j.electacta.2017.06.039.

[43] J. Wang, S. Kaskel, KOH activation of carbon-based materials for energy storage, J. Mater. Chem. 22 (2012) 23710–23725, http://dx.doi.org/10.1039/c2jm34066f.

[44] S.-T. Liu, X.-G. Chen, A.-B. Zhang, et al., Electromagnetic performance of rice husk ash, BioResources 9 (2) (2014), http://dx.doi.org/10.15376/biores.9.2.2328-2340.

[45] M. Zhi, F. Yang, F. Meng, et al., Effects of pore structure on performance of an activated-carbon supercapacitor electrode recycled from scrap waste tires, ACS Sust. Chem.

Eng. 2 (7) (2014) 1592–1598,
http://dx.doi.org/10.1021/sc500336h.

[46] K. Yang, J. Peng, C. Srinivasakannan, et al., Preparation of high surface area activated carbon from coconut shells using microwave heating, Bioresour. Technol. 101 (15) (2010) 6163–6169, http://dx.doi.org/10.1016/j.biortech.2010.03.001.

[47] M. Olivares-Marín, C. Fernández-González, A. Macías-García, et al., Preparation of activated carbons from cherry stones by activation with potassium hydroxide, Appl. Surf. Sci. 252 (17) (2006) 5980–5983, http://dx.doi.org/10.1016/j.apsusc.2005.11.018.

[48] Y. Zhang, Y. Huang, H. Chen, et al., Composition and structure control of ultralight graphene foam for high-performance microwave absorption, Carbon 105 (2016) 438–447, http://dx.doi.org/10.1016/j.carbon.2016.04.070.

[49] Y. Lu, Y. Wang, H. Li, et al., MOF-derived porous Co/C nanocomposites with excellent electromagnetic wave absorption properties, ACS Appl. Mater. Interfaces 7 (24) (2015) 13604–13611, http://dx.doi.org/10.1021/acsami.5b03177.

[50] Y. Zhang, Y. Huang, H.H. Chen, et al., Composition and structure control of ultralight graphene foam for high-performance microwave absorption, Carbon 105 (2016) 438–447, http://dx.doi.org/10.1016/j.carbon.2016.04.070.

[51] R.B. Cevallos Toledo, C.F. Aragón-Tobar, S. Gámez, et al., Reactivation process of activated carbons: effect on the mechanical and adsorptive properties, Molecules 25 (7) (2020), http://dx.doi.org/10.3390/molecules25071681.

[52] O.-W. Achaw, A study of the porosity of activated carbons using the scanning electron microscope, in: D.V. Kazmiruk (Ed.), Scanning Electron Microscopy, Ed.: InTech, 2012.

[53] J. Ramirez-Rico, A. Gutierrez-Pardo, J. Martinez-Fernandez, et al., Thermal conductivity of Fe graphitized wood derived carbon, Mater. Des. 99 (2016) 528–534, http://dx.doi.org/10.1016/j.matdes.2016.03.070.

[54] M. Deraman, Resistivity of carbon from oil palm bunches: percolation theory, J. Phys. D: Appl. Phys. 27 (5) (1994) 1060–1062, http://dx.doi.org/10.1088/0022-3727/27/5/026.

[55] M. Green, L. Tian, P. Xiang, et al., Co2P nanoparticles for microwave absorption, Mater. Today Nano 1 (2018) 1–7, http://dx.doi.org/10.1016/j.mtnano.2018.04.004.

[56] B. Zhao, J. Deng, R. Zhang, et al., Recent advances on the electromagnetic wave absorption properties of Ni based materials, Eng. Sci. 3 (2018) 5–40, http://dx.doi.org/10.30919/es8d735.

[57] S. Gao, Q. An, Z. Xiao, et al., Significant promotion of porous architecture and magnetic Fe_3O_4 NPs inside honeycomb-like carbonaceous composites for enhanced microwave absorption, RSC Adv. 8 (34) (2018) 19011–19023, http://dx.doi.org/10.1039/c8ra00913a.